

Orthogonal Attosecond Control of Solid-State Harmonics by Optical Waveforms and Quantum Geometry Engineering

Zhenjiang Zhao¹, Zhihua Zheng¹, Zhiyi Xu¹, Xing Ran¹, Xiaolong Yao^{1,3,*}, Fangping
Ouyang^{1,2,†}

¹*School of Physical Science and Technology, Xinjiang Key Laboratory of Solid-State
Physics and Devices, Xinjiang University, Urumqi 830017, China*

²*School of Physics, Institute of Quantum Physics, Hunan Key Laboratory for Super-
Microstructure and Ultrafast Process, and Hunan Key Laboratory of Nanophotonics
and Devices, Central South University, Changsha, 410083, China*

³*Beijing Computational Science Research Center, 100193 Beijing, China*

Abstract

High-harmonic generation (HHG) in two-dimensional materials offers a compelling route toward compact extreme ultraviolet sources and probing electron dynamics on the attosecond scale. However, achieving precise control over the emission and disentangling the complex interplay between intraband and interband quantum pathways remains a central challenge. Here, we demonstrate through first-principles simulations that HHG in monolayer WS₂ can be subjected to precise, complementary control by combining all-optical two-color laser fields with mechanical strain engineering. This dual-mode strategy provides unprecedented, orthogonal control over harmonic yield, polarization, and spectral features. We reveal that sculpting the two-

*Contact author: xlyao@xju.edu.cn

†Contact author: ouyangfp06@tsinghua.org.cn

color field's relative phase provides a sub-femtosecond switch for the quantum coherence of electron-hole pairs, thereby maximizing harmonic emission. Crucially, we uncover that tensile strain acts as a powerful amplifier through a dual mechanism - while strain-modified band dispersion enhances the intraband current, a profound reshaping of the Berry curvature (BC) dramatically boosts the anomalous velocity contribution to the interband response. This quantum geometric effect manifests as a robust, linear dependence of the harmonic yield on strain and a significant amplification of the perpendicularly polarized harmonics, providing a clear experimental signature for probing quantum geometric effects. Our findings establish a versatile framework for optimizing solid-state HHG and introduce a powerful all-optical method to map strain and quantum geometric properties of materials, positioning monolayer WS₂ as a model system for exploring attosecond physics at the nexus of bulk and atomic scales.

Keywords: high-harmonic generation, strain engineering, two-color laser, attosecond dynamics, Berry curvature

I. INTRODUCTION.

High-harmonic generation (HHG), a quintessential nonlinear optical process, arises from the interaction of intense laser fields with matter.[1] This phenomenon has garnered significant interest across atomic, molecular, and solid-state systems.[2-9] In solids, the high electron density and lattice periodicity impose complex constraints on electronic structure and momentum, imparting distinct characteristics to the HHG mechanism compared to its gas-phase counterpart.[10-13] These unique solid-state features have spurred the development of compact and efficient high-harmonic sources and hold significant promise for applications in emerging fields such as multi-terahertz electronics and all-optical information processing.[14-16]

Among condensed matter systems, two-dimensional (2D) materials - such as graphene, hexagonal boron nitride, and transition metal dichalcogenides - have emerged as ideal platforms for studying ultrafast electronic dynamics due to their unique symmetries and electronic properties.[5, 9, 17, 18] These materials exhibit a remarkable duality, bridging atomic- and bulk-like responses. For instance, in monolayer hexagonal boron nitride (hBN), when the driving laser field is polarized perpendicular to the material plane, the real-space electron trajectories resemble those in isolated atoms.[9, 19] Conversely, when the laser is polarized in-plane, the response is characteristic of bulk HHG. This duality positions 2D materials as a critical bridge between atomic-scale and condensed matter physics.

Precise control over HHG has been demonstrated by tailoring laser field parameters (e.g., polarization, ellipticity, and waveform) or by modifying material

properties (e.g., applying strain or varying layer numbers).[17, 20, 21] Specifically, two-color laser fields, where the relative phase between the fundamental and second harmonic is controlled, enable sub-femtosecond manipulation of electron trajectories, leading to enhanced harmonic yields and extended cutoff energies. Strain engineering, a powerful tool for tuning material properties, can modify the band structure and break structural symmetries.[22-24] For example, it has been shown that strain-induced modifications to the band structure and BC can enhance both intraband and interband currents, thereby boosting HHG.[8]

Despite this progress, the interplay between intraband and interband contributions to solid-state HHG remains a subject of active debate.[2, 11, 13, 15, 25-27] The relative dominance of these two mechanisms varies significantly with the material system and spectral range, accounting for the diversity of experimental observations. Therefore, a deeper understanding of the factors governing strong-field electron dynamics in 2D materials is crucial. Such knowledge is essential for developing effective control strategies and advancing both attosecond science and condensed matter physics.

In this work, we employ first-principles simulations based on real-time time-dependent density functional theory (rt-TDDFT),[28, 29] as implemented in the octopus code,[30] to systematically investigate the complementary effects of two-color phase modulation and strain engineering on the sub-femtosecond electron dynamics governing HHG in monolayer WS₂ (1L-WS₂). Our results demonstrate that by optimizing the relative phase of the two-color field, we can achieve sub-femtosecond control over electron motion, thereby significantly enhancing HHG efficiency.

Furthermore, by applying strain engineering, we elucidate the underlying physical mechanisms through which modifications to the band structure and BC influence harmonic yields and spectral features. This work provides not only an experimentally feasible strategy for controlling HHG in 2D materials but also new theoretical insights into the quantum dynamics of laser-solid interactions.

II. THEORETICAL AND COMPUTATIONAL METHODOLOGY

To investigate the interaction between intense laser fields and solids from first principles, we employ real-time time-dependent density functional theory (rt-DDFT).[28, 29] This framework is particularly well-suited for capturing the highly nonlinear, non-perturbative response of the electronic system by propagating the electron and current densities in real time. The electronic dynamics are governed by the time-dependent Kohn-Sham (TDKS) equations, expressed in atomic units as

$$i \frac{\partial}{\partial t} \psi_{n\mathbf{k}}(\mathbf{r}, t) = \left[-\frac{1}{2} \nabla^2 + V_{ext}(\mathbf{r}, t) + V_H(\mathbf{r}, t) + V_{xc}(\mathbf{r}, t) \right] \psi_{n\mathbf{k}}(\mathbf{r}, t) \quad (1)$$

Here, $\psi_{n\mathbf{k}}(\mathbf{r}, t)$ is the Kohn-Sham orbital corresponding to band index n and crystal momentum \mathbf{k} . The total electron density is given by $n(\mathbf{r}, t) = \sum_{n,\mathbf{k}}^{occ} |\psi_{n\mathbf{k}}(\mathbf{r}, t)|^2$, where the sum is over all occupied states. The effective potential consists of three terms: $V_H(\mathbf{r}, t)$ is the time-dependent Hartree potential, accounting for the mean-field Coulomb repulsion between electrons; $V_{ext}(\mathbf{r}, t)$ includes both the electron-ion interaction and the external laser field; and $V_{xc}(\mathbf{r}, t)$ is the exchange-correlation (XC) potential, which incorporates all many-body effects beyond the Hartree approximation.

Upon solving the TDKS equations, we obtain the time-dependent macroscopic current density, $\mathbf{J}(t)$, by averaging the microscopic current over the unit cell

$$\mathbf{J}(t) = \frac{1}{\Omega} \int_{\Omega} d^3r \mathbf{j}(\mathbf{r}, t) \quad (2)$$

where Ω is the unit cell volume and the microscopic current density operator $\mathbf{j}(\mathbf{r}, t)$ is defined as

$$\mathbf{j}(\mathbf{r}, t) = -\frac{i}{2} \sum_{n,\mathbf{k}}^{occ} [\psi_{n\mathbf{k}}^*(\mathbf{r}, t) \nabla \psi_{n\mathbf{k}}(\mathbf{r}, t) - \text{c.c.}] \quad (3)$$

The HHG spectrum, $I(\omega)$, is then computed by Fourier transforming the time derivative of the total current density, which is proportional to the far-field emission

$$I(\omega) = |FT[\frac{d\mathbf{J}(t)}{dt}]|^2 \quad (4)$$

Our simulations are performed within the single-active-electron approximation and neglect decoherence and macroscopic propagation effects.

To gain deeper insight into the underlying excitation pathways, such as interband and intraband transitions, we calculate the number of excited electrons, $N_{ex}(t)$. This quantity is determined by projecting the time-evolved Kohn-Sham orbitals, $|\psi_{n\mathbf{k}}(t)\rangle$, onto the manifold of ground-state occupied bands, $\{|\psi_{m\mathbf{k}}(0)\rangle\}$

$$N_{ex}(t) = N_e - \frac{1}{N_k} \sum_{n,m,\mathbf{k}}^{occ} |\langle \psi_{m\mathbf{k}}(0) | \psi_{n\mathbf{k}}(t) \rangle|^2 \quad (5)$$

Here, the second term on the right-hand side represents the population remaining in the ground-state manifold. N_e is the total number of electrons in the system, and N_k is the total number of k-points sampled in the Brillouin zone (BZ).

Numerical simulations are performed using the octopus code,[30] a real-space, real-time implementation of rt-TDDFT. We employ the adiabatic local density approximation (ALDA) for the exchange-correlation functional. The electron-ion interaction is described by norm-conserving Hartwigsen–Goedecker–Hutter (HGH) pseudopotentials.[31] The monolayer is placed in a simulation cell with a vacuum

spacing of 34 Å along the out-of-plane direction. To prevent unphysical reflections from the simulation box boundaries, complex absorbing potentials (CAPs)[32] with a cap height parameter of $\eta = -1.0$ a.u. were placed in 3.0 a.u. regions flanking the material. The TDKS equations are discretized on a real-space grid with a spacing of 0.21 Å. The BZ is sampled using a $36 \times 36 \times 1$ Monkhorst-Pack k-point grid centered at the Γ -point.

The system is driven by a two-color laser field $\mathbf{E}(t)$, linearly polarized along the zigzag direction of the monolayer WS₂ [see Fig. 1(a)]. The field is a superposition of a fundamental pulse and its second harmonic, derived from the total vector potential $\mathbf{A}(t)$,

where $\mathbf{E}(t) = -\frac{\partial \mathbf{A}(t)}{\partial t}$

$$\mathbf{A}(t) = f(t)[\mathbf{A}_0 \cos(\omega_0 t) + \mathbf{A}_1 \cos(\omega_1 t + \Delta\phi)] \quad (6)$$

Both components share a common Gaussian envelope $f(t)$

$$f(t) = \exp\left(-\frac{(t-t_0)^2}{2\tau^2}\right) \quad (7)$$

In these expressions, $\mathbf{A}_0(\omega_0)$ and $\mathbf{A}_1(\omega_1=2\omega_0)$ are the vector potential amplitudes (frequencies) of the fundamental and second-harmonic fields, respectively. For all simulations, the fundamental photon energy is set to $\hbar\omega_0 = 0.517$ eV ($\lambda_0=2400$ nm). The Gaussian pulse envelope is defined by a standard deviation of $\tau=12$ fs and is centered at $t_0=50$ fs. This corresponds to a $1/e$ intensity duration of $2\tau=24$ fs and an intensity full width at half maximum (FWHM) of $2\sqrt{2\ln 2} \cdot \tau \approx 28.3$ fs. The intensity of the fundamental field is fixed at $I_0=10^{12}$ W/cm². The second-harmonic intensity, controlled via \mathbf{A}_1 , and the relative phase, $\Delta\phi$, serve as the key control parameters in our study.

III. RESULTS AND DISCUSSION

Figure 1(a) illustrates the crystal lattice of 1L-WS₂ and schematically depicts the HHG process under a two-color laser field. The electronic band structure, calculated from first principles, is shown in Fig. 1(b). Our calculations, employing the local density approximation (LDA), yield a minimum direct bandgap of 1.7 eV at the K/K' points. While this value is smaller than the experimental gap of 2.0 eV, a common feature of LDA, the functional accurately reproduces the essential dispersion characteristics of the valence and conduction bands, which are critical for modeling electron dynamics.[33] We acknowledge that quantitative aspects, such as the exact harmonic cutoff energy, may be influenced by the underestimated bandgap. However, our key qualitative conclusions concerning the control of carrier dynamics, the effects of symmetry breaking, and the crucial role of the BC are robust, as these phenomena are primarily dictated by the band dispersion and wavefunction topology, which are well-described by the LDA functional. For reference, the Perdew-Burke-Ernzerhof (PBE) functional predicts a slightly larger bandgap, consistent with prior theoretical work.[34] The reciprocal space structure is depicted in Fig. 1(c), with a calculated lattice constant of $a = 3.186 \text{ \AA}$.

To probe the nonlinear optical response, we investigate the influence of the relative phase, $\Delta\varphi$, between the two components of a linearly polarized two-color laser field on HHG in 1L-WS₂. This parameter is known to be a powerful tool for controlling harmonic emission.[9, 17, 35-37] As illustrated by the electric field waveforms in Fig. 2(a), the two-color scheme introduces a pronounced temporal asymmetry controlled by $\Delta\varphi$. While the fundamental pulse ($\beta = 0$) is symmetric (black curve), the synthesized

two-color fields ($\beta = 1$) exhibit strong asymmetry for both $\Delta\phi = 0.7\pi$ (red) and $\Delta\phi = \pi$ (blue). Consequently, while solid-state HHG driven by a single fundamental pulse is insensitive to the carrier-envelope phase, the engineered waveform asymmetry of the two-color field enables precise, phase-dependent control over the harmonic spectrum [Fig. 2(b)].

This broken symmetry has profound consequences for the harmonic polarization. As shown in Figs. 2(c) and 2(d), the two-color field simultaneously generates both odd- and even-order harmonics and allows for the dynamic redistribution of harmonic energy between the parallel (P_x , along the x -direction) and perpendicular (P_y , along the y -direction) polarization components. By performing a polarization decomposition of the harmonic signal, we can disentangle the microscopic origins of the emission. The parallel component (P_x) is overwhelmingly dominant, contributing over 90% of the total intensity, and originates almost exclusively from interband currents - the coherent recombination of laser-driven electron-hole pairs. In contrast, the much weaker perpendicular component (P_y) arises primarily from intraband dynamics - the acceleration of charge carriers within a single band - and exhibits a more sensitive dependence on $\Delta\phi$.^[8] This analysis unequivocally demonstrates that interband transitions are the dominant mechanism governing HHG in 1L-WS₂, a finding rooted in the material's fundamental electronic properties.

The relative phase $\Delta\phi$ is therefore a key parameter for controlling not just the polarization but also the overall efficiency of the HHG process. Figure 2(e) quantifies this dependence by plotting the integrated harmonic yield across different spectral

bands as a function of $\Delta\varphi$. The total yield (orders 1 - 40) and the high-energy plateau yield (orders 4 - 30) exhibit a clear modulation, reaching a maximum at $\Delta\varphi \approx 0.7\pi$ and a minimum near $\Delta\varphi = 0$ and π . We hypothesize that this modulation of HHG efficiency is directly linked to the effective peak intensity of the synthesized laser field, which is itself governed by $\Delta\varphi$.

To test this hypothesis, we systematically calculate the HHG yield as a function of the incident laser pulse intensity, as shown in Fig. 2(f). The results confirm a strong, monotonic dependence - the HHG yield decreases significantly as the laser intensity is reduced. This confirms that $\Delta\varphi$ controls the HHG yield primarily by modulating the effective peak electric field strength of the composite laser pulse; a stronger transient field drives a more efficient harmonic generation process by promoting more electron-hole pair creation and more energetic subsequent recombination.

To further elucidate the microscopic dynamics underlying the harmonic emission, we performed a wavelet time-frequency analysis of the induced electronic current. This technique maps the temporal evolution of the current, $\mathbf{j}(t)$, into a time-frequency domain, $S(t, \omega)$, providing a time-resolved picture of the emission process[38]

$$S(t_0, \omega_0) = \int j(t)w^*(t - t_0, \omega_0)dt \quad (8)$$

Here, $\mathbf{j}(t)$ is the microscopic current corresponding to Equation (3) and $w(t, \omega)$ is the complex conjugate of the mother wavelet. For this analysis, we employ a Gabor wavelet, which provides optimal resolution in both time and frequency

$$w(t, \omega_0) = \left(\frac{1}{\sigma_t \sqrt{2\pi}}\right) \exp\left(-\frac{t^2}{2\sigma_t^2}\right) \exp(i\omega_0 t) \quad (9)$$

where σ_t determines the temporal duration of the wavelet window. The resulting time-

frequency intensity distribution, which is what is plotted, is given by the squared modulus of the transform

$$I(t_0, \omega_0) = |S(t_0, \omega_0)|^2 \quad (10)$$

Figures 3(a) and 3(b) present this analysis for two representative phases, $\Delta\varphi = 0.7\pi$ and $\Delta\varphi = \pi$, respectively, revealing the sub-cycle electron dynamics.

Several key features emerge. First, for both cases, higher-order harmonics are emitted in distinct bursts localized near the extrema of the driving electric field, with the harmonic cutoff energy directly scaling with the peak field amplitude.[2, 39] This observation reinforces our conclusion that $\Delta\varphi$ controls the HHG spectrum by tailoring the transient field strength. Second, the sub-cycle waveform control offered by the two-color field directly sculpts the structure of the harmonic spectrum. For $\Delta\varphi = 0.7\pi$, the field waveform features two adjacent peaks of comparable amplitude within a half-cycle [A_1 and B_1 in Fig. 3(a)]. The emissions from these two events interfere, resulting in a harmonic spectrum with a sharply resolved, discrete structure.[40, 41] Conversely, for $\Delta\varphi = \pi$, the second harmonic constructively interferes to create a single, much stronger field maximum [A_2 in Fig. 3(b)] and weaker secondary features (B_2, C_2). This produces a single, dominant emission burst per half-cycle, leading to a smoother, more continuous harmonic spectrum.

Crucially, in both scenarios, the primary harmonic emission events are locked to the extrema of the laser's vector potential. This specific timing is a definitive signature of HHG governed by interband dynamics, where electron-hole pairs are first created near the field zero-crossing, accelerated by the field, and then driven to recombine and

emit high-energy photons as the vector potential reaches its maximum or minimum.[13]

This time-frequency analysis provides a compelling microscopic picture that fully supports our central conclusion - the HHG process in 1L-WS₂ is dominated by interband transitions, which can be precisely controlled on a sub-femtosecond timescale by the relative phase of a two-color field.

To elucidate the physical mechanism of the phase modulation effect, we analyze the dynamics of electronic excitation. Within the semiclassical acceleration theory, the motion of a Bloch electron under the laser pulse is governed by the time-dependent wave vector, $\mathbf{k}(t) = \mathbf{k}_0 - e[A(t) - A(t_0)]/\hbar$, where \mathbf{k}_0 is the initial wave vector at the electron's birth time t_0 , and $A(t)$ is the vector potential of the two-color field.[42, 43] This framework directly links the electron's trajectory in momentum space to the instantaneous structure of the laser field.

The population of excited electrons, a proxy for the interband transition probability, closely tracks the temporal structure of the vector potential modulus, $|A(t)|$ [Figs. 3(c) and 3(d)]. The dynamics differ markedly with the relative phase, $\Delta\varphi$. For $\Delta\varphi = 0.7\pi$, the $|A(t)|$ waveform exhibits a multi-peaked structure that periodically drives electron excitation, leading to a correspondingly oscillatory rise in the excited electron population. In stark contrast, for $\Delta\varphi = \pi$, constructive interference between the two-color fields reshapes the waveform into a single, dominant primary peak with significantly weaker sub-cycle features. This concentrates the excitation process into a much narrower temporal window, resulting in a single, prominent peak in the excited electron population. These results demonstrate that the sub-cycle structure of the vector

potential, precisely controlled by $\Delta\varphi$, directly governs the temporal profile of electron excitation.

This phase-dependent excitation dynamic is mirrored in the time-resolved occupation of individual electronic orbitals [Figs. 3(e) and 3(f)]. At $\Delta\varphi = 0.7\pi$, the occupation numbers of multiple orbitals - spanning from VBM-5 to the CBM+3 - exhibit pronounced, periodic oscillations. This behavior is characteristic of coherent, Rabi-like cycling between the valence and conduction bands, driven by the periodic strong field.[44] This sustained quantum coherence ensures that recolliding electrons encounter a hole state with a well-defined phase relationship, a condition that is critical for efficient constructive interference and the emission of high-frequency harmonics.

Conversely, at $\Delta\varphi = \pi$, the orbital occupations evolve smoothly, showing a monotonic increase followed by rapid relaxation without the intense oscillations seen at $\Delta\varphi = 0.7\pi$ [Figs. 3(e) and 3(f)]. This rapid decoherence stems from strong non-adiabatic coupling between electronic states induced by the laser field at this specific phase.[45, 46] This coupling facilitates the rapid dissipation of the initial excitation energy across a manifold of electronic states, transforming the coherent hole into a thermalized-like, mixed-state ensemble. The probability of a recolliding electron coherently recombining with such a decohered hole system is drastically reduced, leading to a profound suppression of the HHG yield.

Taken together, these findings reveal a clear microscopic mechanism: $\Delta\varphi = 0.7\pi$ enhances HHG by preserving the quantum coherence of electron-hole dynamics, whereas $\Delta\varphi = \pi$ suppresses it by promoting rapid, non-adiabatic decoherence. This not

only confirms the dominant role of interband currents in the HHG process in WS₂ but also establishes two-color phase control as a powerful tool for manipulating quantum coherence on ultrafast timescales.

Beyond optical control, we investigate strain engineering as an orthogonal means to tune the HHG process.[22, 47-50] As shown in Fig. 4(a), applying biaxial strain has a pronounced effect - tensile strain systematically enhances the HHG yield, while compressive strain suppresses it. A polarization-resolved analysis reveals this effect to be highly anisotropic and provides a clear signature of underlying quantum geometric effects. While compressive strain (-2%) attenuates both polarization components, it particularly quenches the harmonic signal perpendicular to the strain axis (P_y) [Fig. 4(b)]. Conversely, tensile strain (+2%) dramatically amplifies the P_y component [Fig. 4(c)]. This trend is quantified in Fig. 4(d), which shows that tensile strain systematically increases the relative contribution of P_y to the total harmonic power, demonstrating that strain anisotropically reshapes the pathways for harmonic emission.[50]

To understand the microscopic origins of this strain-tuning, particularly the striking amplification of the perpendicular harmonic component, we analyze the strain-induced modifications to the electronic band structure and, crucially, the BC, as shown in Figs. 5. The suppression of HHG under compressive strain can be attributed to two factors visible in the band structure [Fig. 5(a)]. First, the bandgap widens, energetically disfavoring interband transitions. Second, the gap transitions from direct to indirect, which would require momentum-conserving phonon scattering for efficient excitation - a process far too slow to contribute to femtosecond-scale HHG dynamics. In contrast,

tensile strain reduces the direct bandgap, facilitating electron excitation and globally enhancing the HHG yield.

More profoundly, the anisotropic enhancement of the P_y component is a direct manifestation of strain-induced changes in the material's quantum geometry. The BC, shown in Fig. 5(b), acts as an intrinsic, momentum-space pseudo-magnetic field that gives rise to an anomalous velocity component perpendicular to the applied electric field.[51] In monolayer WS₂, strong spin-orbit coupling and broken inversion symmetry endow the K and K' valleys with large BC of opposite sign.[52] Our calculations show that tensile strain, while preserving the C_3 rotational symmetry and thus the valley degeneracy, profoundly reshapes the electronic wavefunctions, leading to a significant modulation of the BC's magnitude and distribution within each valley. This redistribution directly modifies the anomalous velocity, making it anisotropic. To substantiate this mechanism, Table I reveals a clear positive correlation between the integrated BC near the K -valley and the integrated vertical harmonic yield. This correlation provides direct evidence that the BC is a key regulator of high-harmonic generation, confirming that the enhancement of the P_y component is driven by the strain-induced BC modulation.

We attribute the observed amplification of the P_y harmonic component primarily to this strain-induced BC modulation. While strain also introduces a modest anisotropy in the interband transition dipole moments (TDMs), our detailed analysis confirms that this effect is quantitatively insufficient to explain the several-fold increase in the P_y yield.(Fig. 1(b)) Therefore, the dominant mechanism is the enhanced anomalous

velocity, which selectively amplifies the nonlinear current perpendicular to the driving laser's polarization. This establishes the perpendicularly polarized harmonic signal as a sensitive, all-optical probe of strain-modulated quantum geometry in 2D materials.

To elucidate the mechanism connecting strain to the harmonic yield, we computationally investigate the electronic excitation dynamics. Figures 6 presents the time-evolution of the excited electron population under varying strain conditions. Specifically, tensile strain ($\varepsilon = +2\%$) leads to a significantly larger excited electron population compared to both the unstrained ($\varepsilon = 0\%$) and compressively strained ($\varepsilon = -2\%$) cases [Fig. 6(a)]. Conversely, compressive strain markedly suppresses the excitation efficiency. An analysis of the time-dependent orbital occupations reveals the origin of this behavior [Figs. 6(b)-(d)]. In the unstrained case [Fig. 6(b)], occupations near the VBM and CBM evolve smoothly, indicating that transitions are predominantly localized between these frontier bands. Under compressive strain [Fig. 6(c)], oscillations in the VBM occupation are damped, and relaxation is accelerated. This is consistent with the strain-induced shift to an indirect bandgap, which suppresses efficient interband transitions. In sharp contrast, under tensile strain [Fig. 6(d)], the populations of multiple conduction band orbitals (e.g., CBM, CBM+1) increase substantially and persist long after the laser pulse has passed. This sustained population of excited states signifies that tensile strain not only boosts excitation efficiency but also slows the subsequent carrier relaxation. This prolonged lifetime of excited carriers is crucial, as it increases the probability of their recollision with the parent ion - the final, decisive step in high-harmonic generation.

HHG, an advanced nonlinear optical phenomenon, demonstrates immense potential for generating coherent extreme ultraviolet (EUV) radiation and attosecond pulses. This study demonstrates that HHG yields in monolayer WS₂ can be effectively modulated by synergistically combining strain engineering with all-optical phase control, opening a new paradigm for coherent control in ultrafast optics and condensed matter physics. To systematically investigate the governing control mechanisms, we constructed a two-dimensional map of the HHG yield as a function of the two-color relative phase ($\Delta\varphi$) and applied strain (ε) [Fig. 7]. Here, $\Delta\varphi$ provides all-optical control over the driving field, while ε acts as a mechanical parameter that modifies the material's fundamental electronic and quantum geometric properties. In this map, the horizontal axis represents $\Delta\varphi$ (in units of π), and the vertical axis denotes ε (ranging from -2% compressive to +2% tensile). The color scale (yellow to purple) indicates increasing HHG yield. This analysis reveals the independent contributions of strain and phase, as well as their synergistic interaction. First, strain engineering provides an effective knob for modulating the overall yield. The maximum yield, achieved under +2% tensile strain, is 27.6% higher than the maximum yield observed under -2% compressive strain. Compressive strain, therefore, consistently suppresses the HHG output. This modulation is attributed to strain-induced modifications of the electronic band structure and the associated BC, which directly influence the material's nonlinear optical response. Second, the efficacy of this all-optical phase control is strongly dependent on the strain state. Under tensile strain ($\varepsilon = +2\%$), the HHG yield shows high sensitivity to $\Delta\varphi$, peaking at 0.3π and remaining elevated in the 0.3π – 0.7π range. This

indicates that fine-tuned regulation and maximization of HHG are possible via phase control, but only when the material is under optimal tensile stress. Conversely, under unstrained or compressive conditions, the influence of $\Delta\varphi$ on the yield diminishes significantly, resulting in a much flatter modulation profile. This synergistic effect reveals a crucial physical interplay - the two-color phase ($\Delta\varphi$) provides sub-femtosecond control over the electron-hole trajectories to optimize their recollision dynamics. However, this trajectory control is only effective when the material's electronic properties - namely the band structure and BC - are first favorably tuned by tensile strain. In compressed or unstrained states, the intrinsic band topology or interband transition dipoles hinder this phase-controlled optimization, rendering the all-optical control ineffective.

IV. CONCLUSIONS

In this study, we have employed first-principles rt-TDDFT to systematically investigate HHG and the underlying electronic dynamics in monolayer WS₂ under the combined influence of a two-color laser field and mechanical strain. Our results demonstrate that the relative phase ($\Delta\varphi$) of the two-color field provides a precise, sub-femtosecond control knob for manipulating the harmonic yield, spectral features, and polarization. Specifically, a relative phase of $\Delta\varphi = 0.7\pi$ maximizes the harmonic emission efficiency, a condition that correlates with sustained coherence in the electronic transitions. Our analysis further confirms that interband transitions are the dominant HHG mechanism, accounting for over 90% of the total harmonic intensity.

Furthermore, we establish that strain engineering offers a powerful and

complementary method for tuning the material's nonlinear optical response. Applying tensile strain enhances the HHG efficiency and significantly amplifies the perpendicularly polarized harmonic component by strategically modifying the band structure and BC. Conversely, compressive strain suppresses harmonic emission; this is attributed to an increase in the bandgap and a shift toward an indirect-gap character, which collectively inhibit the requisite electronic excitations. Critically, the synergistic interaction between tensile strain and a specific relative phase difference maximizes the HHG yield. This synergistic effect is rooted in distinct physical mechanisms. strain-induced lattice distortion directly alters the material's band structure and quantum geometric properties, while the relative phase enables sub-femtosecond control of the electronic trajectories, thereby maximizing constructive interference.

Collectively, these findings elucidate the quantum dynamical pathways of solid-state HHG in monolayer WS₂ and provide a robust theoretical framework for designing efficient and highly tunable solid-state EUV light sources. By combining the distinct and complementary mechanisms of all-optical control and strain engineering, this work opens promising avenues for advanced applications in ultrafast spectroscopy and attosecond science.

ACKNOWLEDGMENTS

This work is sponsored by the Natural Science Foundation of Xinjiang Uygur Autonomous Region (Grant No. 2023D01D03 and 2022D01C689), the Xinjiang University Outstanding Graduate Student Innovation Project (Grant No.

- [1] A. Gorlach, M. E. Tzur, M. Birk, M. Krüger, N. Rivera, O. Cohen, and I. Kaminer, High-harmonic generation driven by quantum light, *Nat. Phys.* **19**, 1689-1696 (2023).
- [2] S. Ghimire, A. D. DiChiara, E. Sistrunk, P. Agostini, L. F. DiMauro, and D. A. Reis, Observation of high-order harmonic generation in a bulk crystal, *Nat. Phys.* **7**, 138-141 (2011).
- [3] Y. S. You, David A. Reis, and S. Ghimire, Anisotropic high-harmonic generation in bulk crystals, *Nat. Phys.* **13**, 345-349 (2017).
- [4] T. Higuchi, C. Heide, K. Ullmann, H. B. Weber, and P. Hommelhoff, Light-field-driven currents in graphene, *Nature* **550**, 224-228 (2017).
- [5] N. Yoshikawa, T. Tamaya, and K. Tanaka, High-harmonic generation in graphene enhanced by elliptically polarized light excitation, *Science* **356**, 736-738 (2017).
- [6] T. Kanai, S. Minemoto, and H. Sakai, Quantum interference during high-order harmonic generation from aligned molecules, *Nature* **435**, 470-474 (2005).
- [7] Z.-Y. Chen, and R. Qin, Strong-field nonlinear optical properties of monolayer black phosphorus, *Nanoscale* **11**, 16377-16383 (2019).
- [8] M.-X. Guan, C. Lian, S.-Q. Hu, H. Liu, S.-J. Zhang, J. Zhang, and S. Meng, Cooperative evolution of intraband and interband excitations for high-harmonic generation in strained MoS₂, *Phys. Rev. B* **99**, 184306 (2019).
- [9] G. Le Breton, A. Rubio, and N. Tancogne-Dejean, High-harmonic generation from few-layer hexagonal boron nitride: Evolution from monolayer to bulk response, *Phys. Rev. B* **98**, 165308 (2018).
- [10] S. Ghimire, G. Ndabashimiye, A. D. DiChiara, E. Sistrunk, M. I. Stockman, P. Agostini, L. F. DiMauro, and D. A. Reis, Strong-field and attosecond physics in solids, *J. Phys. B: At. Mol. Opt. Phys.* **47**, 204030 (2014).
- [11] T. T. Luu, M. Garg, S. Y. Kruchinin, A. Moulet, M. T. Hassan, and E. Goulielmakis, Extreme ultraviolet high-harmonic spectroscopy of solids, *Nature* **521**, 498-502 (2015).
- [12] M. Korbman, S. Y. Kruchinin, and V. S. Yakovlev, Quantum beats in the polarization response of a dielectric to intense few-cycle laser pulses, *New J. Phys.* **15**, 013006 (2013).
- [13] M. Wu, S. Ghimire, D. A. Reis, K. J. Schafer, and M. B. Gaarde, High-harmonic generation from Bloch electrons in solids, *Phys. Rev. A* **91**, 043839 (2015).
- [14] J. Rivera-Dean, P. Stammer, A. S. Maxwell, T. Lamprou, E. Pisanty, P. Tzallas, M. Lewenstein, and M. F. Ciappina, Quantum-optical analysis of high-order harmonic

generation in H_2^+ molecules, Phys. Rev. A **109**, 033706 (2024).

[15] M. Garg, M. Zhan, T. T. Luu, H. Lakhotia, T. Klostermann, A. Guggenmos, and E. Goulielmakis, Multi-petahertz electronic metrology, Nature **538**, 359-363 (2016).

[16] C. Heide, Y. Kobayashi, S. R. U. Haque, and S. Ghimire, Ultrafast high-harmonic spectroscopy of solids, Nat. Phys. **20**, 1546-1557 (2024).

[17] M. Guan, S. Hu, H. Zhao, C. Lian, and S. Meng, Toward attosecond control of electron dynamics in two-dimensional materials, Appl. Phys. Lett. **116**, 043101 (2020).

[18] J. Zhang, O. Neufeld, N. Tancogne-Dejean, I. T. Lu, H. Hübener, U. De Giovannini, and A. Rubio, Enhanced high harmonic efficiency through phonon-assisted photodoping effect, npj Comput. Mater. **10**, 202 (2024).

[19] N. Tancogne-Dejean, and A. Rubio, Atomic-like high-harmonic generation from two-dimensional materials, Sci. Adv. **4**, eaao5207 (2018).

[20] X. Y. Zhang, S. Q. Hu, M. X. Guan, and S. Meng, Optimizing attosecond-pulse generation in solids by modulating electronic dynamics with a monochromatic laser field, Phys. Rev. A **111**, 023521 (2025).

[21] X. S. Kong, X. Y. Wu, L. Geng, and W. D. Yu, Strain effects on high-harmonic generation in monolayer hexagonal boron nitride, Front. Phys. **10**, 1032671 (2022).

[22] S. Yang, Y. Chen, and C. Jiang, Strain engineering of two-dimensional materials: Methods, properties, and applications, InfoMat **3**, 397-420 (2021).

[23] N. Rana, M. S. Mrudul, and G. Dixit, High-harmonic generation from strain-engineered graphene for polarization tailoring, Phys. Rev. B **110**, 054103 (2024).

[24] Z. Peng, X. Chen, Y. Fan, D. J. Srolovitz, and D. Lei, Strain engineering of 2D semiconductors and graphene: from strain fields to band-structure tuning and photonic applications, Light Sci. Appl. **9**, 190 (2020).

[25] C. R. McDonald, G. Vampa, P. B. Corkum, and T. Brabec, Interband Bloch oscillation mechanism for high-harmonic generation in semiconductor crystals, Phys. Rev. A **92**, 033845 (2015).

[26] T. Tamaya, A. Ishikawa, T. Ogawa, and K. Tanaka, Diabatic Mechanisms of Higher-Order Harmonic Generation in Solid-State Materials under High-Intensity Electric Fields, Phys. Rev. Lett. **116**, 016601 (2016).

[27] T. Higuchi, M. I. Stockman, and P. Hommelhoff, Strong-Field Perspective on High-Harmonic Radiation from Bulk Solids, Phys. Rev. Lett. **113**, 213901 (2014).

[28] E. Runge, and E. K. U. Gross, Density-Functional Theory for Time-Dependent Systems, Phys. Rev. Lett. **52**, 997-1000 (1984).

[29] R. van Leeuwen, Mapping from Densities to Potentials in Time-Dependent Density-Functional Theory, Phys. Rev. Lett. **82**, 3863-3866 (1999).

[30] X. Andrade, D. Strubbe, U. De Giovannini, A. H. Larsen, M. J. T. Oliveira, J. Alberdi-Rodriguez, A. Varas, I. Theophilou, N. Helbig, M. J. Verstraete, L. Stella, F. Nogueira, A. Aspuru-Guzik, A. Castro, M. A. L. Marques, and A. Rubio, Real-space grids and the Octopus code as tools for the development of new simulation approaches for electronic systems, Phys. Chem. Chem. Phys. **17**, 31371-31396 (2015).

[31] C. Hartwigsen, S. Goedecker, and J. Hutter, Relativistic separable dual-space

Gaussian pseudopotentials from H to Rn, Phys. Rev. B **58**, 3641-3662 (1998).

[32] U. De Giovannini, A. H. Larsen, and A. Rubio, Modeling electron dynamics coupled to continuum states in finite volumes with absorbing boundaries, Eur. Phys. J. B **88**, 56 (2015).

[33] D. Waroquiers, A. Lherbier, A. Miglio, M. Stankovski, S. Poncé, M. J. T. Oliveira, M. Giantomassi, G.-M. Rignanese, and X. Gonze, Band widths and gaps from the Tran-Blaha functional: Comparison with many-body perturbation theory, Phys. Rev. B **87**, 075121 (2013).

[34] R. Rodrigues Pela, C. Vona, S. Lubeck, B. Alex, I. Gonzalez Oliva, and C. Draxl, Critical assessment of G0W0 calculations for 2D materials: the example of monolayer MoS₂, npj Comput. Mater. **10**, 77 (2024).

[35] N. Tancogne-Dejean, O. D. Mücke, F. X. Kärtner, and A. Rubio, Ellipticity dependence of high-harmonic generation in solids originating from coupled intraband and interband dynamics, Nat. Commun. **8**, 745 (2017).

[36] T.-J. Shao, L.-J. Lü, J.-Q. Liu, and X.-B. Bian, Quantum path interferences and selection in interband solid high-order harmonic generation in MgO crystals, Phys. Rev. A **101**, 053421 (2020).

[37] X. Liu, L. Geng, X.-S. Kong, J. Zhang, Y.-K. Fang, and L.-Y. Peng, Theoretical investigations of high harmonic generation in the Weyl semimetal WP₂, Phys. Rev. B **111**, 184314 (2025).

[38] X.-M. Tong, and S.-I. Chu, Probing the spectral and temporal structures of high-order harmonic generation in intense laser pulses, Phys. Rev. A **61**, 021802 (2000).

[39] G.-R. Jia, X.-H. Huang, and X.-B. Bian, Nonadiabatic redshifts in high-order harmonic generation from solids, Opt. Express **25**, 23654-23662 (2017).

[40] J. J. Carrera, X. M. Tong, and S.-I. Chu, Creation and control of a single coherent attosecond xuv pulse by few-cycle intense laser pulses, Phys. Rev. A **74**, 023404 (2006).

[41] C. A. Haworth, L. E. Chipperfield, J. S. Robinson, P. L. Knight, J. P. Marangos, and J. W. G. Tisch, Half-cycle cutoffs in harmonic spectra and robust carrier-envelope phase retrieval, Nat. Phys. **3**, 52-57 (2007).

[42] B. Huang, L. Du, Q. Yi, L. Yang, J. Li, L. Miao, C. Zhao, and S. Wen, Bulk-structured PtSe₂ for femtosecond fiber laser mode-locking, Opt. Express **27**, 2604-2611 (2019).

[43] S. Y. Kruchinin, F. Krausz, and V. S. Yakovlev, Colloquium: Strong-field phenomena in periodic systems, Rev. Mod. Phys. **90**, 021002 (2018).

[44] L. Yue, R. Hollinger, C. B. Uzundal, B. Nebgen, Z. Gan, E. Najafidehaghani, A. George, C. Spielmann, D. Kartashov, A. Turchanin; et al., Signatures of Multiband Effects in High-Harmonic Generation in Monolayer MoS₂, Phys. Rev. Lett. **129**, 147401 (2022).

[45] D. Azoury, M. Krüger, B. D. Bruner, O. Smirnova, and N. Dudovich, Direct measurement of Coulomb-laser coupling, Sci. Rep. **11**, 495 (2021).

[46] D.-A. Trieu, T.-T. D. Nguyen, T.-D. D. Nguyen, T. Tran, V.-H. Le, and N.-L. Phan, Analytically controlling the laser-induced electron phase in sub-cycle motion, Phys. Rev. A **110**, L021101 (2024).

[47] Y. Qi, M. A. Sadi, D. Hu, M. Zheng, Z. Wu, Y. Jiang, and Y. P. Chen, Recent Progress in Strain Engineering on Van der Waals 2D Materials: Tunable Electrical, Electrochemical, Magnetic, and Optical Properties, *Adv. Mater.* **35**, 2205714 (2023).

[48] Z. Liu, M. Amani, S. Najmaei, Q. Xu, X. Zou, W. Zhou, T. Yu, C. Qiu, A. G. Birdwell, F. J. Crowne; et al., Strain and structure heterogeneity in MoS₂ atomic layers grown by chemical vapour deposition, *Nat. Commun.* **5**, 5246 (2014).

[49] S. Roy, X. Yang, and J. Gao, Biaxial strain tuned upconversion photoluminescence of monolayer WS₂, *Sci. Rep.* **14**, 3860 (2024).

[50] S. Yang, W. Chen, B. Sa, Z. Guo, J. Zheng, J. Pei, and H. Zhan, Strain-Dependent Band Splitting and Spin-Flip Dynamics in Monolayer WS₂, *Nano Lett.* **23**, 3070-3077 (2023).

[51] S. Zhang, Y. Wang, Q. Zeng, J. Shen, X. Zheng, J. Yang, Z. Wang, C. Xi, B. Wang, M. Zhou; et al., Scaling of Berry-curvature monopole dominated large linear positive magnetoresistance, *Proc. Natl. Acad. Sci. U.S.A.* **119**, e2208505119 (2022).

[52] D. Xiao, G.-B. Liu, W. Feng, X. Xu, and W. Yao, Coupled Spin and Valley Physics in Monolayers of MoS₂ and Other Group-VI Dichalcogenides, *Phys. Rev. Lett.* **108**, 196802 (2012).

Figures:

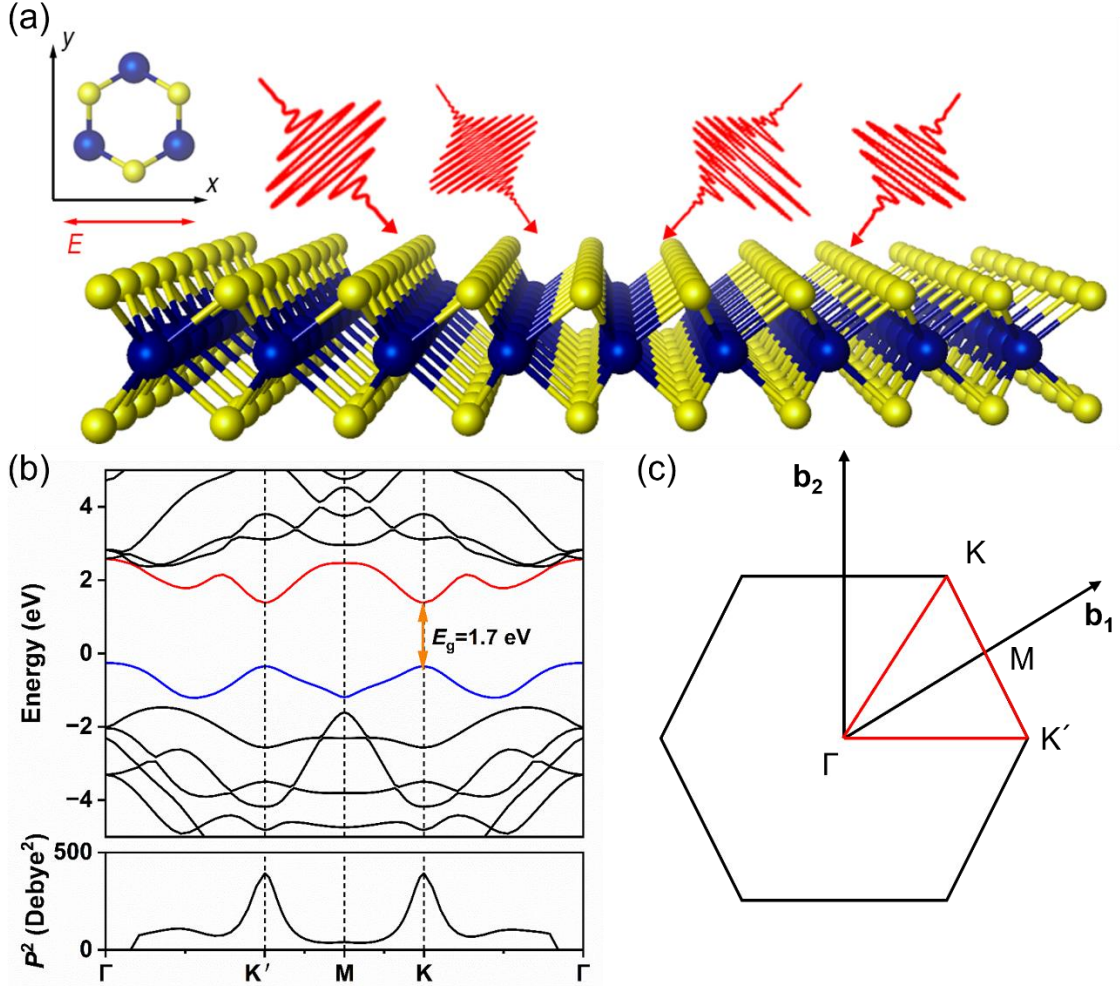


FIG. 1. (a) Schematic of a monolayer (1L) WS₂ interacting with a two-color laser field. The electric field (E) is polarized along the x -axis (zigzag direction). The inset shows the top-down atomic structure. (b) Electronic band structure (top) and the corresponding squared transition dipole moment (P^2) (bottom) for 1L-WS₂. The valence band maximum (VBM, blue) and conduction band minimum (CBM, red) are highlighted, showing a direct band gap (E_g) of approximately 1.7 eV at the K and K' valleys. (c) The first Brillouin zone of WS₂, showing the high-symmetry points Γ , M, K, and K', along with the reciprocal lattice vectors \mathbf{b}_1 and \mathbf{b}_2 .

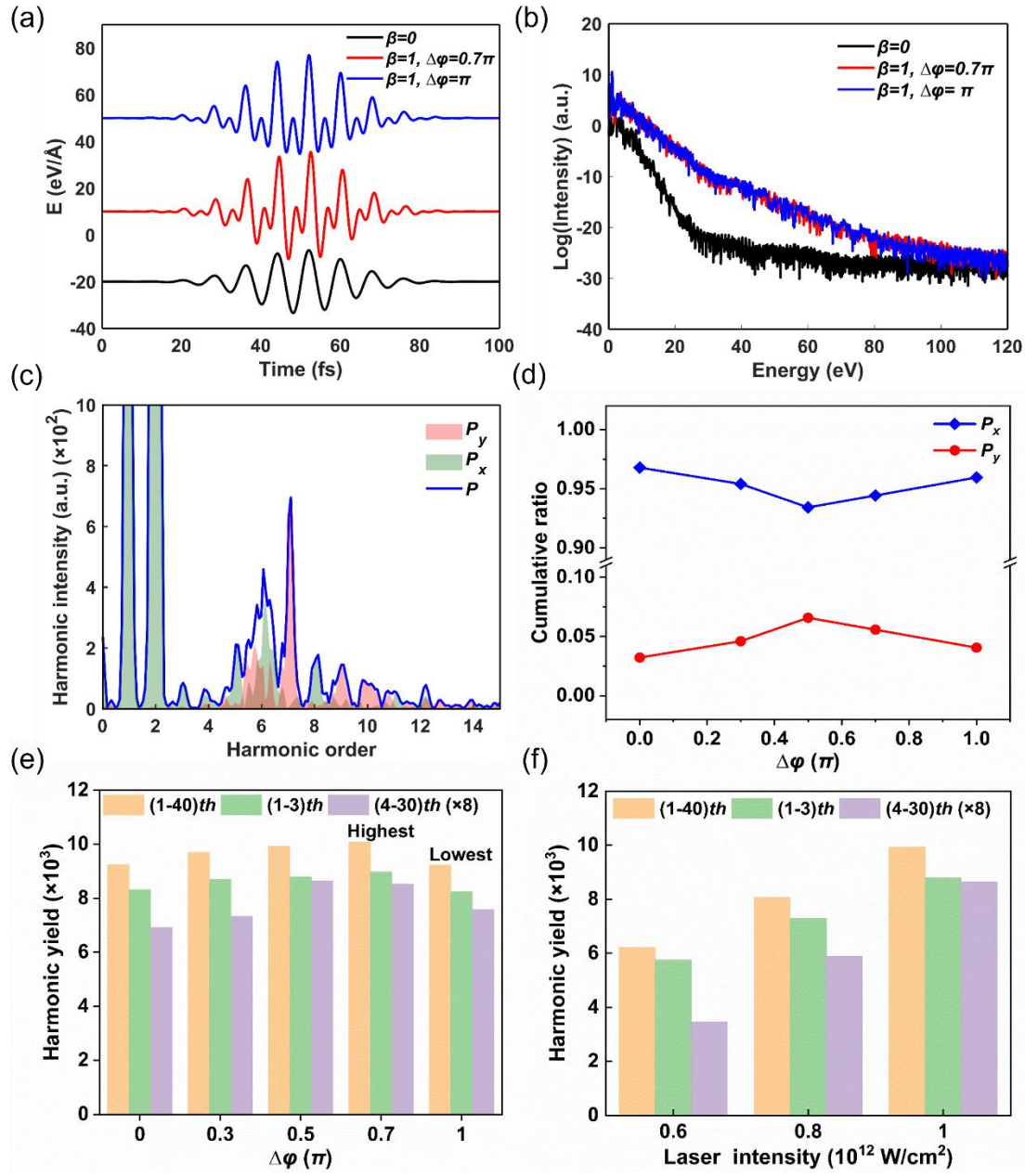


FIG. 2. Control of high-harmonic generation (HHG) using a two-color laser field. The field consists of a fundamental frequency and its second harmonic, with a relative phase $\Delta\varphi$ and field strength ratio β . (a) Temporal profiles of the driving laser field for a single-color pulse ($\beta=0$) and two-color pulses with $\Delta\varphi = 0.7\pi$ and $\Delta\varphi = \pi$. Waveforms are vertically shifted for clarity. (b) Corresponding HHG spectra, plotted on a logarithmic scale. (c) Decomposition of the harmonic spectrum for the $\Delta\varphi = 0.7\pi$ case into components parallel (P_x) and perpendicular (P_y) to the fundamental's polarization,

along with the total intensity (P). (d) Fractional contribution of the parallel and perpendicular components to the total harmonic power for the five relative phases shown. (e) Integrated harmonic yield as a function of the relative phase, $\Delta\varphi$, for the total spectrum (orders 1-40), low-order harmonics (1-3), and high-order harmonics (4-30). (f) Integrated harmonic yield as a function of peak laser intensity. In (e) and (f), the high-order harmonic yield is scaled by a factor of 8 for clarity.

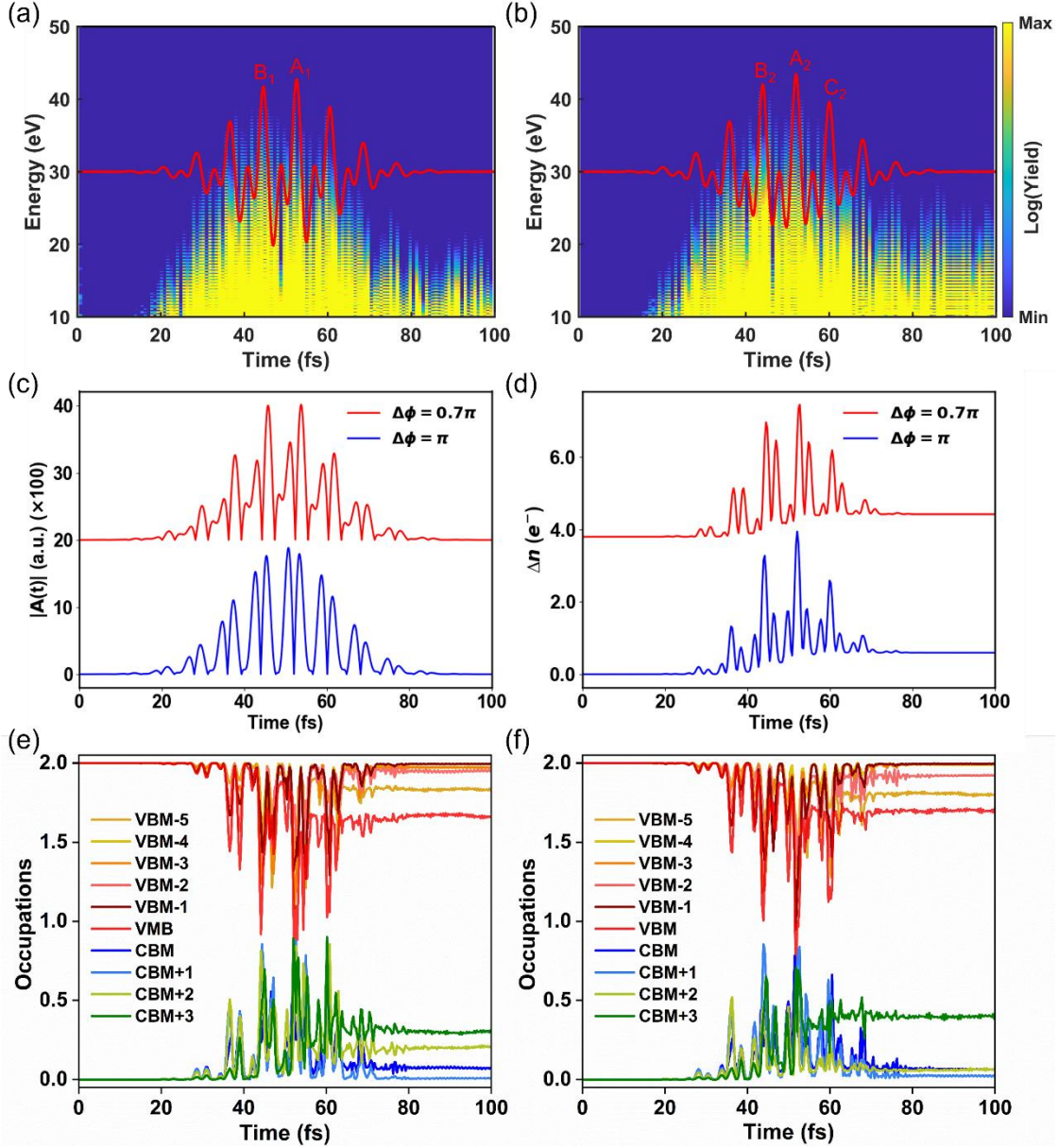


FIG. 3. Time-resolved electron dynamics under two-color fields. (a, b) Time-frequency analysis of the harmonic emission for $\Delta\phi = 0.7\pi$ (a) and $\Delta\phi = \pi$ (b). The overlaid red curves show the driving electric field, and the labels (e.g., A_1 , B_1) denote distinct emission bursts. Unless otherwise stated, the laser intensity is $1.0 \times 10^{12} \text{ W/cm}^2$ and $\beta=1$. (c) Temporal profile of the vector potential amplitude, $|A(t)|$, and (d) time evolution of the total excited electron population, Δn , for relative phases of $\Delta\phi = 0.7\pi$ (red) and $\Delta\phi = \pi$ (blue). For visibility, the $\Delta\phi = 0.7\pi$ curves in (c) and (d) are vertically offset by +20 and +3.8, respectively. (e, f) Time-dependent occupations of specific valence (VBM) and conduction (CBM) bands for (e) $\Delta\phi = 0.7\pi$ and (f) $\Delta\phi = \pi$.

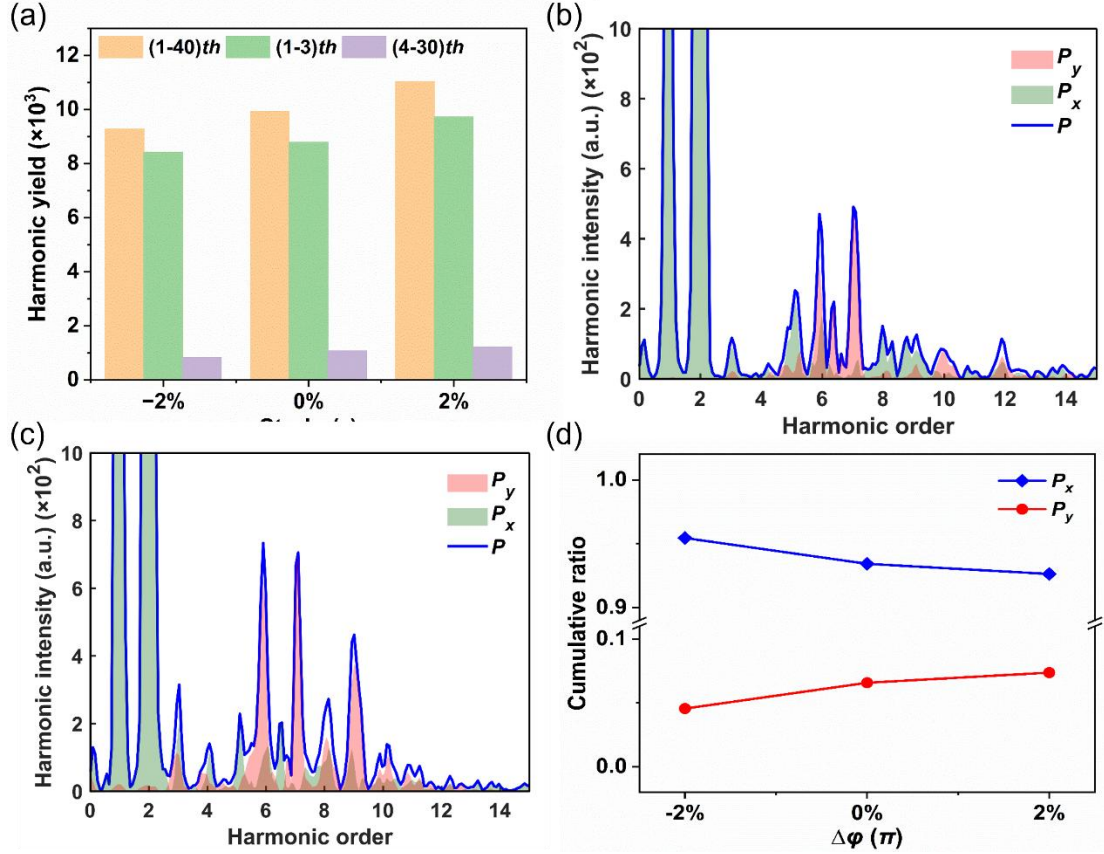


FIG. 4. Effect of biaxial strain (ϵ) on high-harmonic generation. (a) Integrated harmonic yield as a function of strain for the total spectrum [(1-40)th], low-order harmonics [(1-3)th], and high-order harmonics [(4-30)th]. The yield values are scaled by 10^3 . (b, c) Polarization-resolved HHG spectra under (b) compressive strain (-2%) and (c) tensile strain (+2%). (d) Fractional power distribution between the harmonic components parallel (P_x) and perpendicular (P_y) to the driving laser's polarization.

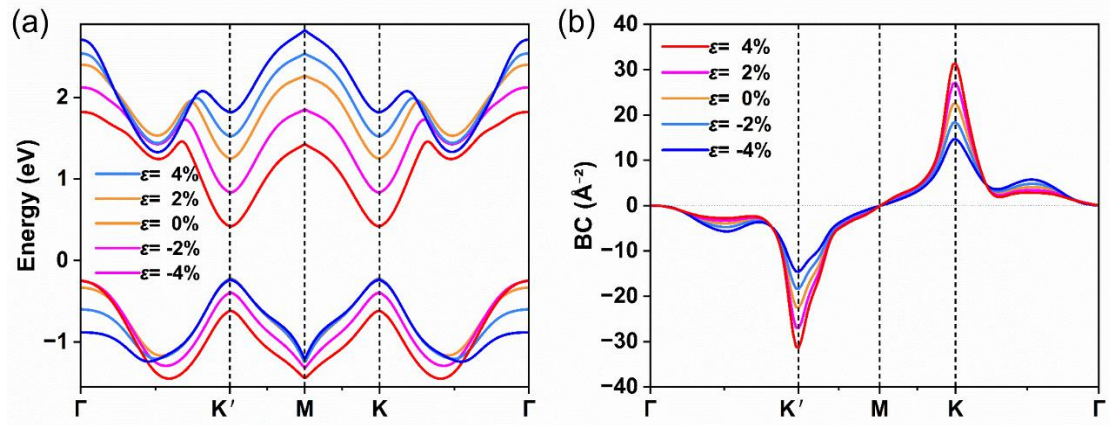


FIG. 5. Effect of biaxial strain (ϵ) on the electronic properties of monolayer WS₂. (a) Electronic band structure and (b) the corresponding Berry curvature (BC) calculated along the high-symmetry path Γ -K'-M-K- Γ . The calculations are shown for strain values ranging from -4% (compressive) to +4% (tensile).

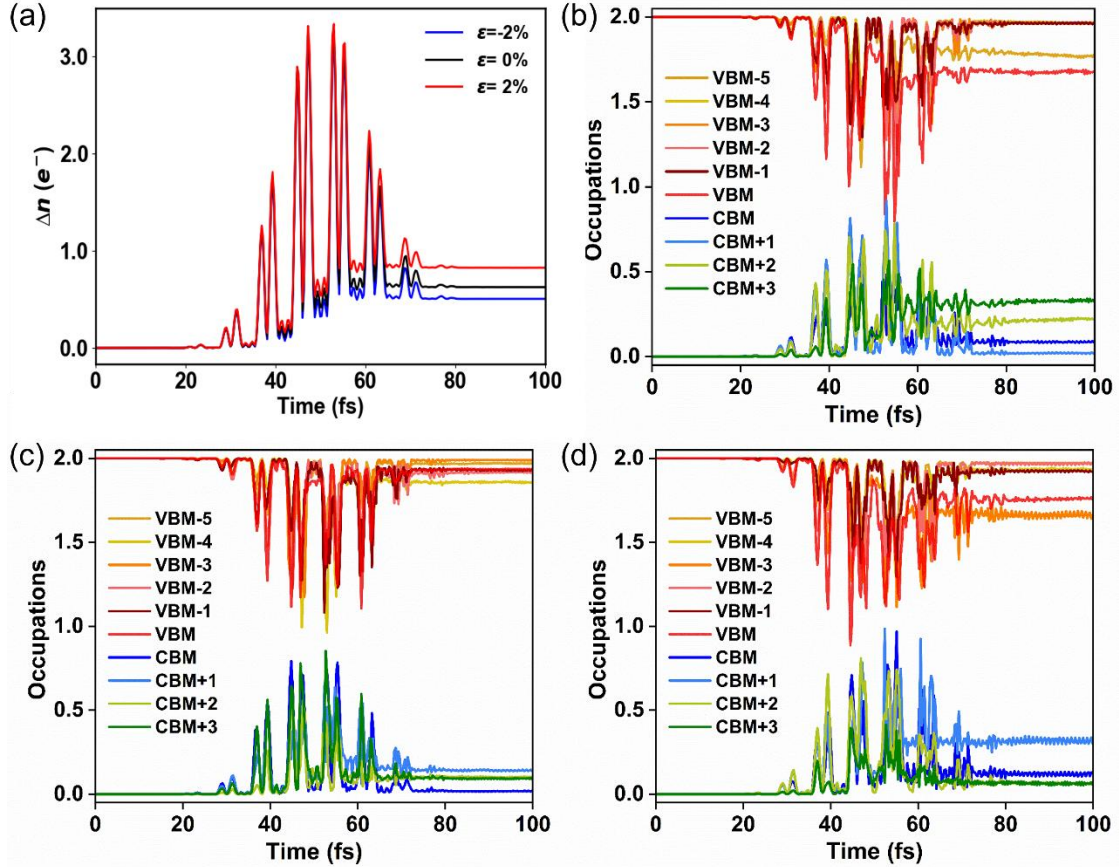


FIG. 6. Effect of biaxial strain on time-resolved electron dynamics. (a) Time evolution of the total excited electron population (Δn) for compressive (-2%), zero (0), and tensile ($+2\%$) strain. (b-d) The corresponding state-resolved occupations in the valence (VBM) and conduction (CBM) bands under conditions of (b) zero strain, (c) -2% compressive strain, and (d) $+2\%$ tensile strain.

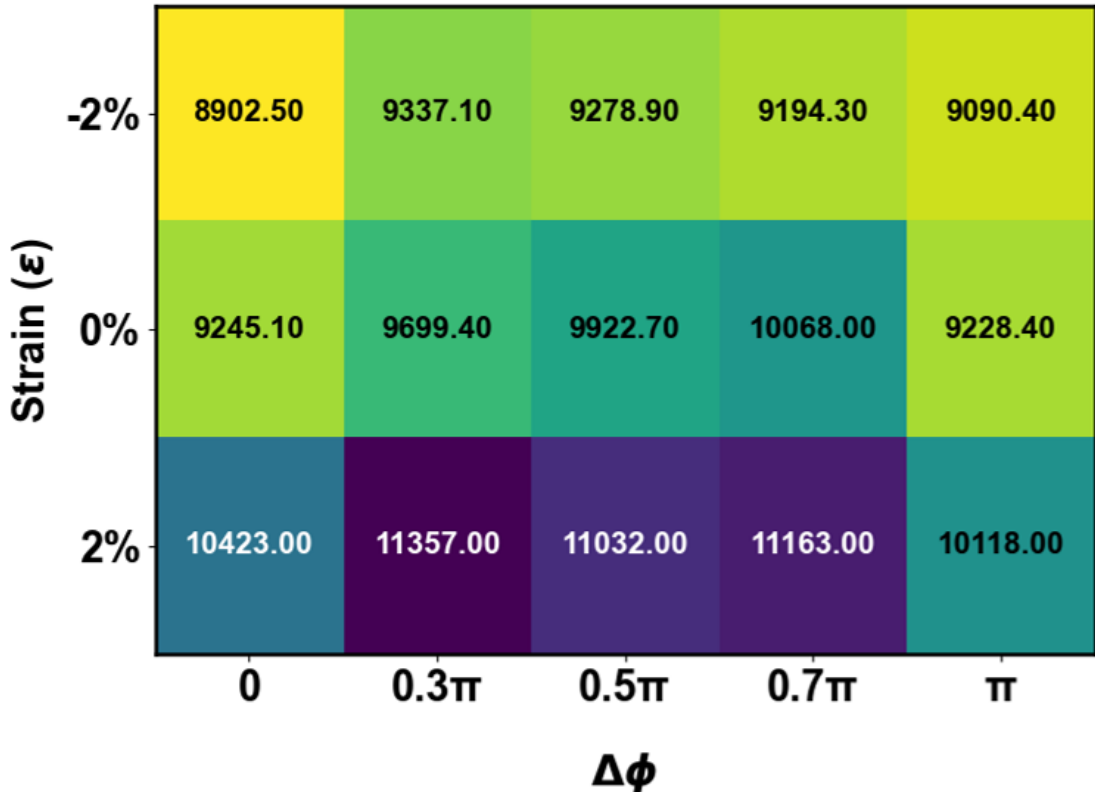


FIG. 7. Synergistic regulation of harmonic anisotropy. The 2D heatmap plots the harmonic anisotropy (indicated by the numerical values) as a function of uniaxial strain (ε) (y-axis) and the all-optical phase difference ($\Delta\phi$) (x-axis). The plot demonstrates that the anisotropy can be precisely controlled by the interplay of both parameters. The maximum value (11357.00) is observed at 2% tensile strain and a phase difference of 0.3π , while the minimum value (8902.50) occurs at -2% compressive strain and a phase difference of 0.

Tables:

TABLE I. Comparison of Berry curvature (BC) and harmonic yield. The table lists three distinct values for BC (in \AA^{-2}) and their corresponding harmonic yields (in a.u.).

BC (\AA^{-2})	Harmonic yield (a.u.)
18.24	1467.0
22.36	2285.1
26.86	2894.6